

Polarization of RRAT J2325-0530 with FAST

Le Yang ^{1,2}, Zhi-Fu Gao^{2,4}, Zhi-Gang Wen^{2,4}, Li-Yun Zhang ^{1,3,4}, Baoda Li¹, and Hao Shan²
¹ College of Physics, Guizhou University, Guiyang 550025, China
² Xinjiang Astronomical Observatory, Chinese Academy of Sciences, Urumqi 830011, China; zhifugao@xao.ac.cn, wenzhigang@xao.ac.cn, liy_zhang@hotmail.com

³ International Centre of Supernovae, Yunnan Key Laboratory, Kunming 650216, China

International Centre of Supernovae, Yunnan Key Laboratory, Kunming 650216, China Received 2025 June 9; revised 2025 August 2; accepted 2025 August 18; published 2025 October 23

Abstract

We report on high-sensitivity polarization measurements of the rotating radio transient (RRAT) J2325–0530 conducted with the Five-hundred-meter Aperture Spherical radio Telescope. Using single-pulse search techniques and full-Stokes parameter analysis, we comprehensively explore the source's emission characteristics. The observations reveal three distinct pulse profile types—single-peaked, double-peaked, and multi-peaked—with the multi-peaked category displaying prominent polarization reversals (mean linear polarization fraction of $27.5\% \pm 0.3\%$) and broader pulse widths (7.50 ± 0.82). The relative pulse energy distribution follows a power-law trend and exhibits a strong positive correlation with pulse width (r = 0.80). Through analysis of orthogonal polarization mode transitions, we suggest that the emission likely results from the interplay of multi-scale magnetospheric processes in the polar cap region. Future multi-wavelength campaigns could further test the distinctiveness of this source's emission mechanism. Overall, our findings enhance the current understanding of RRATs' complex emission behavior and inform the broader study of pulsar magnetospheric dynamics.

Key words: (stars:) pulsars: individual (J2325-0530) - polarization - radiation mechanisms: general

1. Introduction

Rotating radio transients (RRATs), first identified in 2006 by McLaughlin et al. through reanalysis of Parkes Multibeam Pulsar Survey data (McLaughlin et al. 2006), represent a unique subclass of pulsars characterized by sporadic, shortduration radio bursts. These bursts typically last between 2 and 30 ms, with interpulse intervals ranging from seconds to hours, yet they maintain underlying periodicities from 41.5 ms to 7.7 s (Zhang et al. 2007). RRATs are distinguished by their surface magnetic field strengths, which span from 10¹¹ to 10^{13} Gauss (G) (Abhishek et al. 2022), and their extreme nulling fractions exceeding 99%, rendering them undetectable by conventional Fourier folding methods (Burke-Spolaor & Bailes 2010; Keane et al. 2011). To date, the RRATalog⁵ has cataloged 117 confirmed RRATs, with population estimates suggesting over 300 such objects (Cui et al. 2017; Patel et al. 2018; Tyul'bashev et al. 2018a, 2018b, 2022; Good et al. 2021; Han et al. 2021; Abhishek et al. 2022; Bezuidenhout et al. 2022; Samodurov et al. 2022, 2023; Dong et al. 2023; Zhou et al. 2023). Despite nearly two decades of research since their discovery, the radiation mechanisms of RRATs remain incompletely understood, highlighting the need for more sensitive observations and detailed analyses to unravel their complex emission behaviors.

Since their discovery in 2006, RRATs have been studied for nearly two decades, yet their emission mechanisms remain unresolved. Two primary interpretations dominate the literature. The first posits that RRATs exhibit bimodal emission, alternating between a nulling state with no detectable radiation and a bursting state where their emission resembles that of ordinary pulsars (Zhang et al. 2007). The second interpretation suggests that RRATs are inherently weak pulsars, with their apparent nulling states arising from emission below detection thresholds, punctuated by sporadic bright pulses (Weltevrede et al. 2006). Recent observations from the Five-hundred-meter Aperture Spherical radio Telescope (FAST) lend support to the latter view, indicating that most RRATs are either weak pulsars with intermittent strong pulses or extreme nulling pulsars (Zhou et al. 2023).

The polarization properties of RRATs offer critical insights into their emission physics. As radio signals propagate, their polarization encodes information about the source's magnetic field geometry and radiation mechanisms. Studies of polarization can distinguish between orthogonal modes (X-mode and O-mode), test predictions of the Rotating Vector Model (RVM), and reveal interactions between emission modes (Wang et al. 2014). However, such measurements demand exceptional sensitivity due to the faint and sporadic nature of RRAT pulses. The FAST telescope has uniquely enabled these observations, as demonstrated by the polarization analysis of RRAT J1819-1458, which revealed an S-shaped position angle

⁴ Corresponding authors. These authors contributed equally to this work.

https://rratalog.github.io/rratalog/

Table 1
Basic Parameters of RRAT J2325-0530

Parameter	Value
R.A. (J2000)	23:25:15.3(1)
Decl. (J2000)	-05:30:39(4)
Period, $P(s)$	0.868735115026(9)
Period derivative, \dot{P} (s s ⁻¹)	$1.029(2) \times 10^{-15}$
DM (pc cm $^{-3}$)	14.966(7)
Surface magnetic field, B_s (G)	1.0×10^{12}
Spin-down power, \dot{E} (erg s ⁻¹)	6.2×10^{31}
Characteristic age, τ (Myr)	13.4

Note. Measured parameters of RRAT J2325-0530 are from discovery observations.

curve with orthogonal jumps, consistent with the RVM (Karastergiou et al. 2009).

RRAT J2325-0530 was discovered through the GBT 350 MHz drift scan and the Green Bank North Celestial Cap Pulsar Survey (Karako-Argaman et al. 2015). Its fundamental properties, including period, dispersion measure (DM), and spin-down parameters, are summarized in Table 1. Multiple studies have been conducted on this source.

Subsequent studies have significantly refined our understanding of this source. In 2016, Meyers et al. (2016) observed RRAT J2325–0530 with the Long Wavelength Array, reporting a revised DM of 14.960 \pm 0.003 pc cm $^{-3}$ and a burst rate of 50 hr $^{-1}$ at 32 MHz, while confirming its period (0.870 s). A major leap forward came in 2019, when Meyers et al. (2019) performed simultaneous multi-frequency observations using the MWA (154 MHz) and Parkes (1.4 GHz). Their work revealed distinct burst rates (73 \pm 7 hr $^{-1}$ and 43 \pm 5 hr $^{-1}$, respectively), characterized the source's spectral index and scintillation properties, and provided the first polarization profile and rotation measure estimate (RM_{ISM} = 3.8 \pm 0.1 rad m $^{-2}$). Additionally, they demonstrated that the waiting time distribution of RRAT J2325 -0530 bursts is consistent with a Poisson process.

Further refinements were achieved by Kravtsov et al. (2020) using the UTP-2 telescope, which measured a pulse width of 45 ± 5 ms, flux density of 55 ± 28 mJy, and a higher burst rate of $103 \pm 51 \, \mathrm{hr}^{-1}$, alongside updated DM and period values. Despite these advances, prior studies have not systematically explored the single-pulse emission dynamics or polarization position angle variations of RRAT J2325–0530.

The most recent observations of RRAT J2325–0530 were conducted in 2020 using the UTP-2 telescope (Kravtsov et al. 2020), which measured key parameters including a pulse width FWHM = 45 ± 5 ms, flux density of $S = 55 \pm 28$ mJy, burst rate of 103 ± 51 hr⁻¹, dispersion measure of DM = 14.954 ± 0.010 pc cm⁻³, and period of P = 0.868735115 s.

Although these and previous studies have successfully refined various parameters through multi-band observations, they have not adequately addressed two critical aspects: (1) the detailed characteristics of single-pulse emissions and (2) the properties of polarization position angles. Our observations with FAST overcome these limitations by leveraging its unparalleled sensitivity. This enables the first detailed study of single-pulse polarization properties, yielding insights into the source's emission geometry and magnetospheric physics.

This paper presents a comprehensive investigation of the polarized emission properties of RRAT J2325-0530 using single-pulse observations from the FAST telescope. The remainder of this study is organized as follows. First, we describe our observational strategy and data reduction methodology in Section 2, detailing the specific approaches used to process the high-sensitivity FAST data. The results of our analysis are then presented in Section 3, where we examine the single-pulse polarization characteristics and their implications for understanding the emission mechanism. In Section 4, we contextualize these findings within the broader framework of RRAT emission models, comparing our results with previous multi-wavelength observations. Finally, Section 5 synthesizes our key discoveries and outlines promising directions for future research, particularly highlighting how the enhanced capabilities of FAST can further advance our understanding of transient radio phenomena.

2. Observations and Data Reduction

The observational data were obtained from targeted observations of RRAT J2325–0530 using the FAST on 2021 October 25, with a total integration time of 3000 s. The observations utilized the central beam of the 19-beam receiver, covering the frequency range of $1000-1500\,\mathrm{MHz}$, and were recorded with 4096 frequency channels and a sampling interval of $49.152\,\mu\mathrm{s}$. Prior to the science observations, a pulsed noise diode signal with a period of $0.1006632960\,\mathrm{s}$ was recorded for polarization calibration.

During the observation, the FAST backend recorded raw voltage products, including the auto-correlations (AA and BB) of the orthogonal linear polarization channels and the real (CR) and imaginary (CI) parts of their cross-correlations. These raw products were subsequently used to compute the full Stokes parameters (I, Q, U, and V) during offline processing.

The initial data processing adopted the published DM of 14.966 pc cm⁻³ from the pulsar ephemeris (Karako-Argaman et al. 2015). We used DSPSR⁶ (van Straten & Bailes 2011) to coherently de-disperse the data and fold them at the known period, producing high time-resolution pulse profiles for

⁶ https://github.com/psrsoft/dspsr

subsequent polarization calibration and analysis with PSRCHIVE.

Radio frequency interference mitigation was performed using the paz tool from the PSRCHIVE package⁷ (Hotan et al. 2004), followed by manual excision using pazi. Polarization calibration was carried out with pac, based on the recorded noise diode signal. The resulting calibration is consistent with that reported by Meyers et al. (2019), confirming the reliability of our processing pipeline.

The rotation measure (RM) was determined using the rmfit utility in PSRCHIVE. To isolate the interstellar contribution, we subtracted the ionospheric RM component calculated with ionFR. The resulting interstellar rotation measure is RM_{ISM} = 3.83 ± 1.75 rad m⁻², in agreement with the previous estimate of 3.8 ± 0.1 rad m⁻² by Meyers et al. (2019).

All Stokes data products were generated using 4096 phase bins to maintain high temporal resolution. For further analysis and visualization, we developed custom Python scripts employing the NumPy and Matplotlib libraries. This robust and well-validated data reduction pipeline enables a high-fidelity characterization of RRAT J2325-0530's single-pulse polarization properties, which we present in the subsequent sections.

3. Results

3.1. Pulse Continuity Statistics

The integrated pulse profile of a pulsar, formed through averaging numerous single pulses, stabilizes when sufficient pulses are accumulated. However, individual pulses display unique characteristics in their profile morphology, energy intensity, pulse width, and peak longitude, making single-pulse analysis essential for understanding the underlying physics.

Our analysis began by calculating the rms of the off-pulse region for each single pulse, using three times this rms value as the detection threshold. Through visual inspection of all 3453 period windows, we ultimately confirmed 146 valid single pulses. Figure 1 displays these pulses in rotational phase sequence, with intensities quantified by SNR. Subsequently, we computed the rms of the SNR values for all single pulses and classified them into strong and weak pulses using a threshold of five times the rms value. This analysis resulted in the identification of 50 strong pulses and 96 weak pulses.

Based on the continuity of single pulses, we categorized them into five types: isolated single rotations, two consecutive rotations, three consecutive rotations, four consecutive rotations, and five consecutive rotations. Figure 2 shows an example of four consecutive rotations, with detailed statistics presented in Figure 3. The analysis reveals that single pulses are predominantly isolated single rotations and two

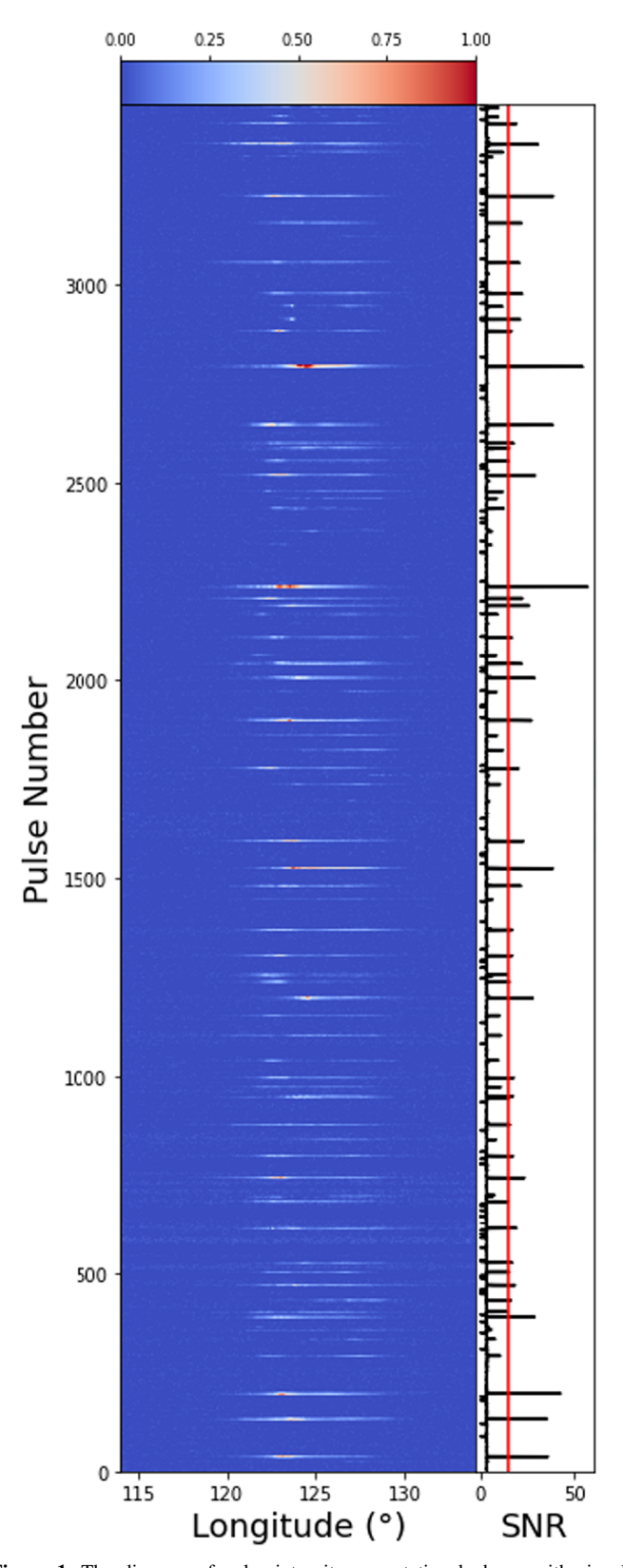


Figure 1. The diagram of pulse intensity vs. rotational phase, with signal strength quantified by the SNR.

https://github.com/psrsoft/psrchive

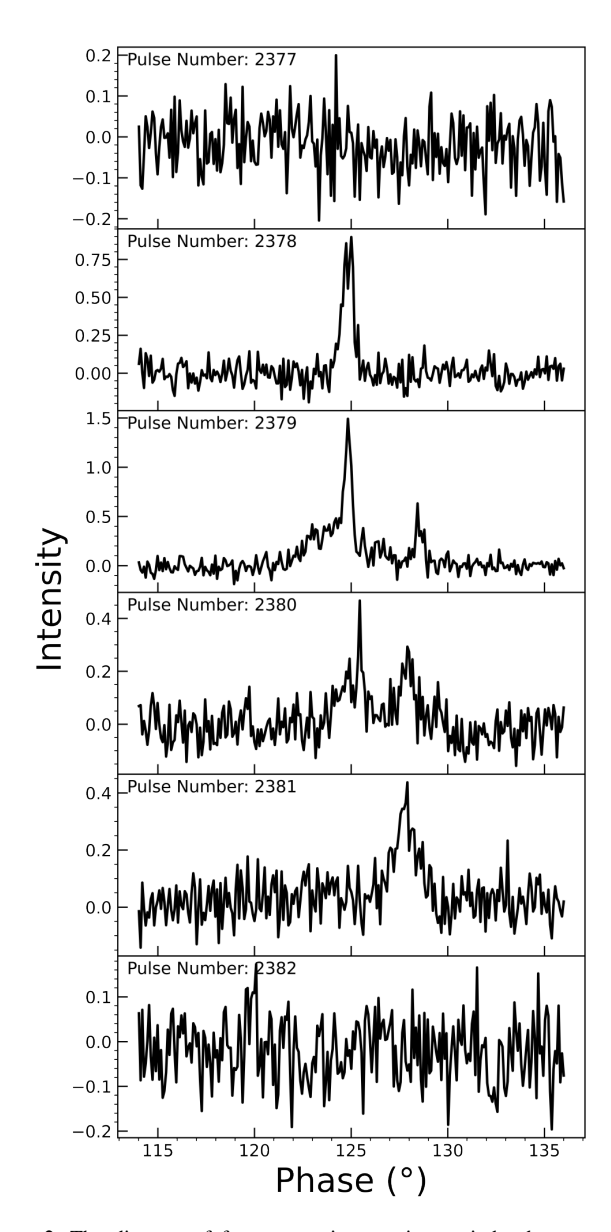


Figure 2. The diagram of four successive rotation periods, demonstrating detectable emission in all consecutive pulses.

consecutive rotations, with a smaller number of three and four consecutive rotations. Only one instance of five consecutive rotations was detected.

During the 50 minutes observation with FAST, we detected a total of 146 single pulses, corresponding to a burst window occupancy of 4.23%, corresponding to a burst rate of approximately 175 hr⁻¹. This rate is significantly higher than that reported by Meyers et al. (2019) using the Parkes telescope at 1.4 GHz. The discrepancy is primarily attributed to the superior sensitivity of FAST, which allows the detection of weak pulses that may be missed by Parkes. When restricting the analysis to the 50 strongest pulses, the inferred burst rate

drops to $60 \, hr^{-1}$, consistent with the Parkes results. These findings reaffirm that RRAT J2325-0530 exhibits highly intermittent radio emission, consistent with previous observations of other RRATs (McLaughlin et al. 2006).

Current research on RRAT emission mechanisms presents several competing hypotheses. Yuen (2024) proposes a common physical origin between RRATs and pulse nulling phenomena, suggesting these may represent different manifestations of similar underlying processes. Supporting evidence comes from Hsu et al. (2023), whose detailed study of RRAT J0628+0909 revealed complex radiation properties during nulling states that may bridge the observational gap between classical RRATs and nulling pulsars. An alternative interpretation by Zhou et al. (2023) posits that some RRATs may represent the extreme end of the nulling pulsar population.

Further insights emerge from Zhang et al. (2024)'s observations of RRAT J1913+1330, which demonstrated nulling-pulsar-like intermittency in its emission patterns. Their analysis suggests this behavior may stem from instabilities in electron-positron pair production above the polar cap region, coupled with dynamic variations in coherent emission sites—mechanisms previously invoked to explain nulling pulsar behavior. Contrastingly, polarization studies of RRAT J1854 +0306 by Guo et al. (2024) indicate that despite superficial intermittency, its fundamental radiation processes resemble those of ordinary pulsars.

The collective evidence strongly supports an intrinsic connection between RRATs and nulling pulsars, though the precise nature of their relationship remains unclear. Key unanswered questions persist regarding: (1) whether these represent distinct populations or points on an observational continuum, (2) the physical drivers of their intermittent emission, and (3) the role of magnetospheric conditions in producing their varied radiation characteristics. Resolution of these questions requires coordinated multi-wavelength observations coupled with advanced theoretical modeling.

3.2. Polarization Characteristics of a Single Pulse

We performed full-Stokes polarization profile analysis for 146 detectable single pulses, measuring the linear polarization degree (L/I) and circular polarization degree (V/I) for each pulse. Notably, some single pulses in Figure 4 exhibit clear microstructure features, which are discussed in detail in Section 3.6. Figure 4 presents representative polarization profiles of several strong pulses, showing the distribution of polarization position angle (PA), as well as characteristic profiles of both linear and circular polarization components. Figure 5 shows the statistical distributions of PA, L/I, and V/I for all single pulses, including the "S"-shaped fit curve based on the RVM model, and the calculated average linear

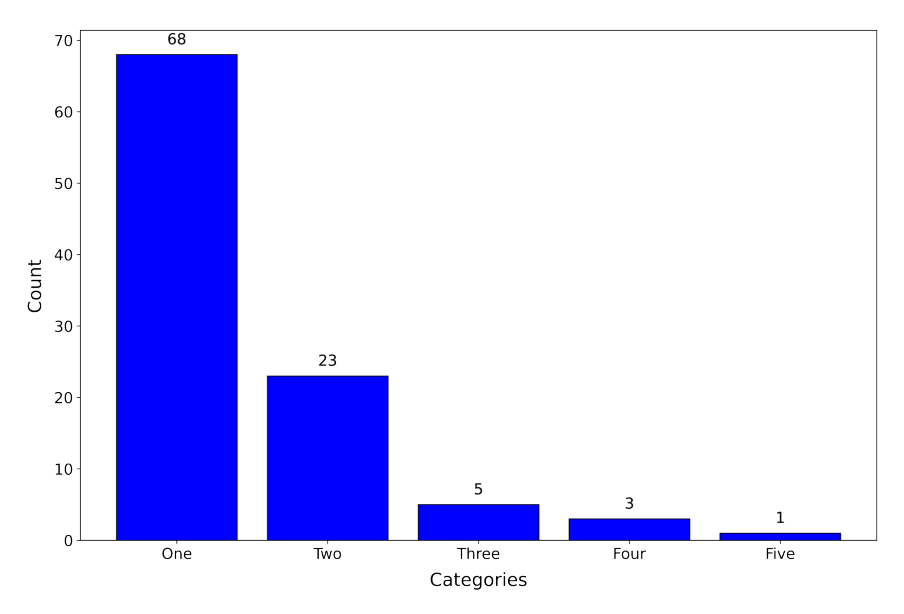


Figure 3. The bar chart of consecutive pulse frequencies (1–5 rotations), with event counts (68, 23, 5, 3, 1) labeled above bars and Poisson errors, showing exponential decrease with sequence length.

polarization degree (28.15% \pm 0.23%) and average circular polarization degree ($-5.22\% \pm 0.23\%$).

Evidently, the polarization position angles (PAs) do not follow the characteristic S-shaped curve predicted by the RVM (Radhakrishnan & Cooke 1969), and a detailed discussion of this discrepancy is presented in Section 3.3. Significant deviations from the average PA distribution are observed in some single pulses, which may reflect variations in magnetospheric plasma conditions (Philippov et al. 2020) and the influence of propagation effects (Barnard & Arons 1986; Blaskiewicz et al. 1991; Gangadhara 2005; Beskin & Philippov 2012). As shown in Figure 5, the linear polarization degree (L/I) of certain pulses can reach up to 100%, while the overall average values are $28.15\% \pm 0.23\%$ (linear) and $-5.22\% \pm 0.23\%$ (circular). A comparative analysis with the 1.4 GHz observations by Meyers et al. (2019) shows good agreement in the polarization degree distributions. However, the pulse morphology distinctions identified in our study could not be resolved in their lower time-resolution data.

3.3. Integrated Pulse Profile Analysis

The integrated pulse profile and its polarization characteristics provide crucial insights into the radiation processes within pulsar magnetospheres. Each pulsar possesses a unique integrated profile, which is obtained through averaging of individual single pulses. As the number of accumulated single pulses increases sufficiently, the integrated profile gradually stabilizes and converges to a characteristic shape.

Figure 6 presents the integrated pulse profiles from all detected single pulses during the observation period, along with the 146 pulses exhibiting detectable signals. Comparative

analysis reveals that the profile in panel (b) displays significantly smoother characteristics than panel (a), with more continuous PA curves-features that are representative of typical emission properties from strong pulses.

Both profiles display a general S-shaped inflection near 125° phase longitude. However, the PA curve deviates significantly from the predictions of the rotating vector model (RVM; Radhakrishnan & Cooke 1969) and cannot be adequately fitted. This result is consistent with the findings of Meyers et al. (2019), who also reported deviations from the RVM model for RRAT J2325–0530. This suggests that RRAT J2325–0530's emission likely originates from complex, multiscale magnetospheric processes occurring near the polar cap region, rather than following the simple geometry assumed by the RVM.

3.4. Energy Distribution

Due to the lack of flux calibration files, we analyzed the pulse energy distribution using relative energies following the method proposed by Ritchings (1976). The reference energy $\langle E \rangle$ was obtained from the integrated intensity within the onpulse window of the mean profile averaged over 146 burst pulses. This window was then applied uniformly to all 3453 pulse periods, calculating the relative energy for each period as $E_i/\langle E \rangle$.

To investigate the energy distribution characteristics of burst pulses, we fitted the burst pulse energy histogram with a power-law model (see Figure 7). The chi-squared value of $\chi^2 = 18.61$ with 15 degrees of freedom indicates that this model describes the observed data well, consistent with the

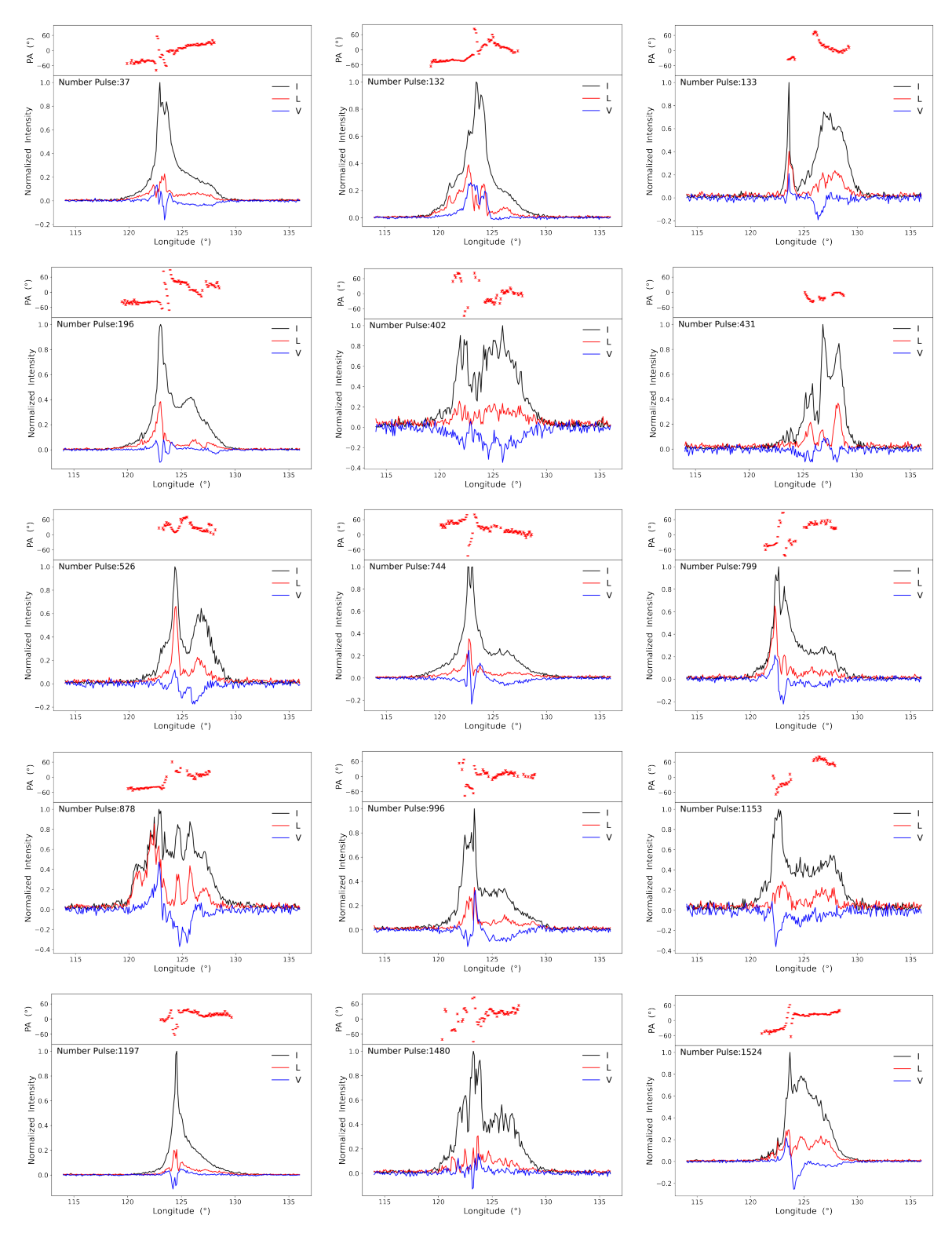


Figure 4. Polarization profiles of selected strong pulses. Red dots show observed PAs. Black curves: total intensity; red curves: linear polarization; blue curves: circular polarization. Pulse numbers are labeled in each panel.

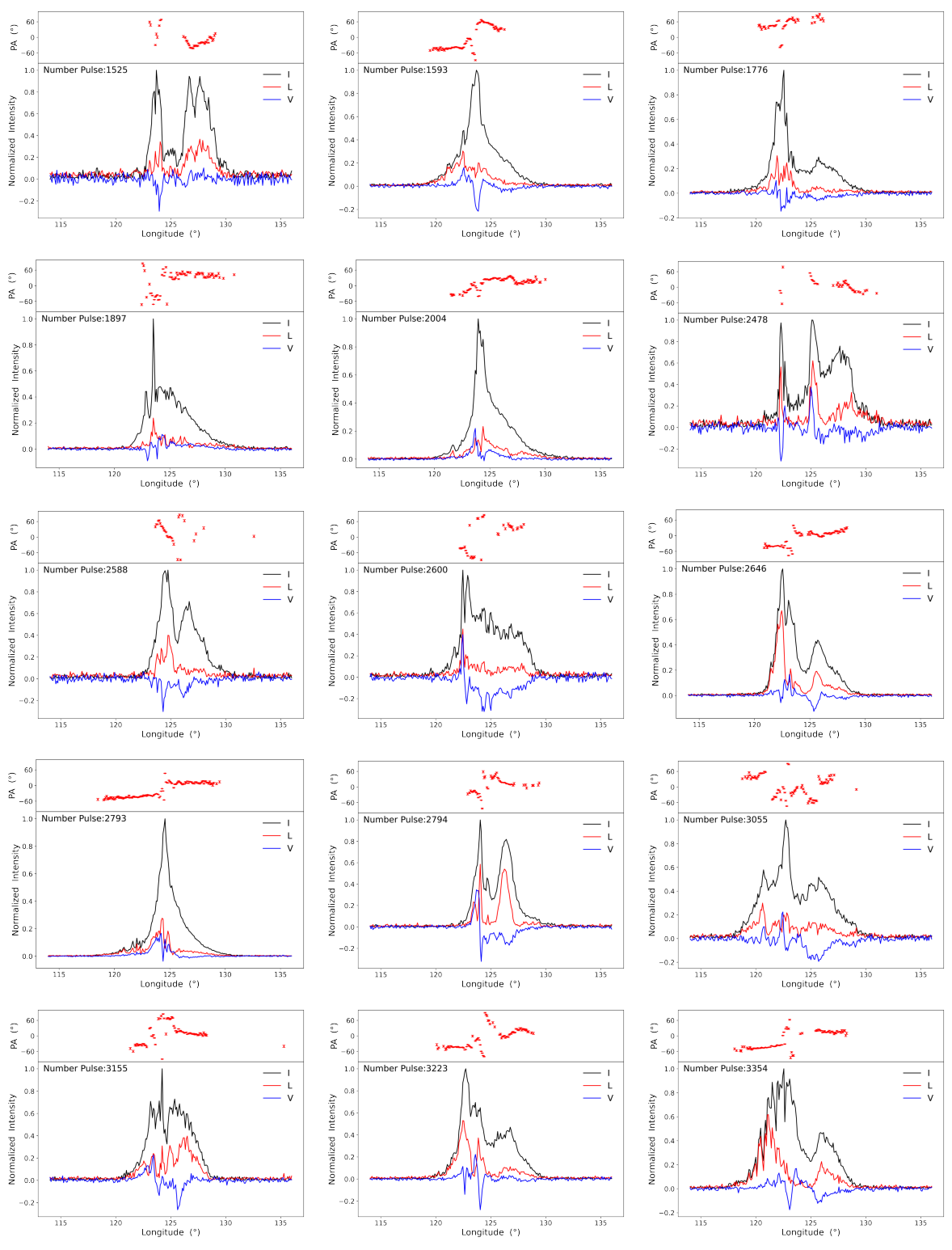


Figure 4. (Continued.)

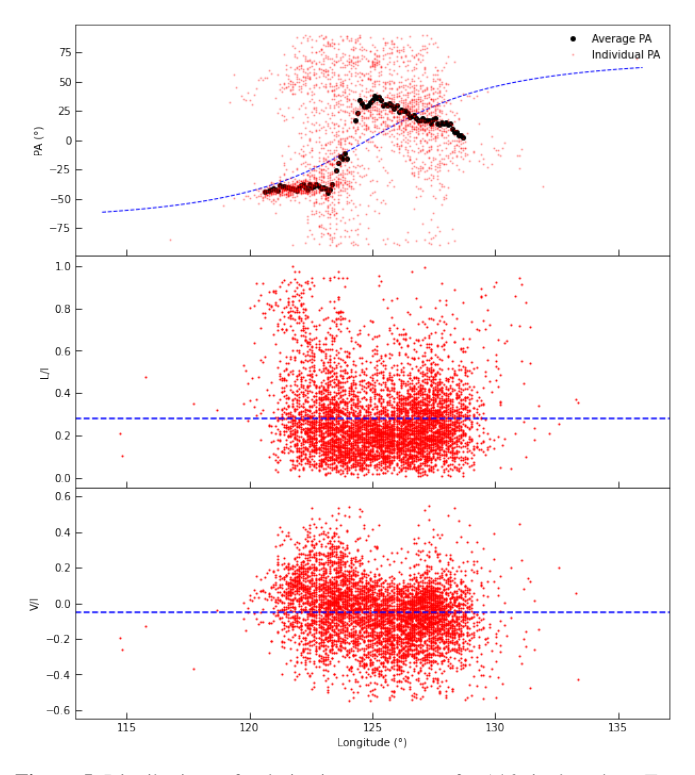


Figure 5. Distributions of polarization parameters for 146 single pulses. Top: PAs; middle: L/I; bottom: V/I. Dashed lines mark average values $(28.15\% \pm 0.23\%$ for L/I, $-5.22\% \pm 0.23\%$ for V/I) and the fitting curves of the Rotating Vector Model (RVM). PA measurements require linear polarization intensity $>3\sigma_L$.

typical long-tailed energy distribution seen in pulsars where most pulses have low energy and only a few have high energy.

3.5. Waiting Time Distribution

In our study of the waiting time (i.e., the time interval between successive burst pulses), we found that the burst emission of RRAT J2325-0530 appears to occur in an irregular manner. We therefore performed a statistical analysis of the waiting time distribution, as shown in Figure 8. The results demonstrate that the waiting time follows an exponential decay. Following the method used by Cordes (2013), we assume that each burst pulse is an independent event. Under this assumption, the waiting time Δt between bursts can be described by a Poisson process, where the probability of a burst occurring within interval Δt is given by $P(\Delta t) = \lambda e^{-\lambda \Delta t}$, where λ is the average occurrence rate. A chi-squared goodness-of-fit test yielded $\chi^2 = 3.54$ with 4 degrees of freedom, indicating an excellent fit between the exponential model and the observed data. The exponential decay function has a time constant of $\lambda = 0.051 \pm 0.005$, implying that on average, one burst is detected every $\sim 20 \, \text{s}$. This corresponds to a burst rate of $184 \pm 18 \,\mathrm{hr}^{-1}$, which agrees well with our initial rate estimation.

The energy storage-release model proposed by Cordes (2013) predicts that the energy of burst pulses should correlate with the duration of the preceding null. However, our analysis of RRAT J2325-0530 shows no significant correlation between burst energy and null duration (Spearman correlation coefficient $\rho=0.12,\ p=0.34$), posing a challenge to this model. Additionally, periodicity checks on pulse sequence numbers reveal no evidence of periodic bursting behavior.

These findings suggest that the radio emission mechanism of RRAT J2325-0530 may differ from that of conventional pulsars. Its non-periodic burst behavior is consistent with the sporadic emission characteristics initially identified in RRATs by McLaughlin et al. (2006).

3.6. Microstructure

Figure 6(b) shows that the integrated pulse profile exhibits no significant microstructural features within the effective pulse window, consistent with the conclusion of Chen et al. (2022) that the averaging process can wash out microstructures visible in individual pulses. We investigated the microstructure of single pulses in RRAT J2325–0530 and selected pulse number 950 as a representative case. The pulse profile and its autocorrelation function (ACF) are shown in Figure 9(a) and (b), respectively, while the Fourier power spectral density (PSD) of the pulse and the power spectral density (ADP) of the ACF for determining quasi-periodicity are shown in Figure 9(c) and (d). The results show that regularly spaced peaks in the ACF confirm the presence of prominent microstructures with quasi-periodicity.

Based on ACF analysis (Lange et al. 1998; Chen et al. 2022), the following parameters were obtained: (1) the time lag of the first slope change (first-order cutoff) in the ACF corresponds to a micropulse width of $\tau_{\mu}=0.42\pm0.06$ ms; (2) the time lag of the second slope change (second-order cutoff) indicates a typical subpulse width of $\tau_s=1.27\pm0.06$ ms. In addition, the time lags of the first and second subpulse-related peaks correspond to a microstructure periodicity of $P_{\mu}=0.85\pm0.06$ ms and a subpulse separation of $P_2=1.70\pm0.06$ ms, respectively, and the frequency peaks in the PSD and ADP are consistent with those obtained from the ACF analysis. The uncertainty of 0.06 ms is determined by the effective time resolution $t_{\rm eff}=\sqrt{t_{\rm samp}^2+t_{\rm DM}^2}$, where the dispersion broadening across channels is $t_{\rm DM}=34.49~\mu s$.

We find that the micropulse width τ_{μ} and the microstructure periodicity P_{μ} follow the empirical relations proposed by Kramer et al. (2024), i.e., $\tau_{\mu} \approx 0.5 P_{\mu}$ and $P_{\mu} \approx 10^{-3} P$, where P is the rotation period. Furthermore, we detected quasiperiodic microstructural features in a total of eight single pulses.

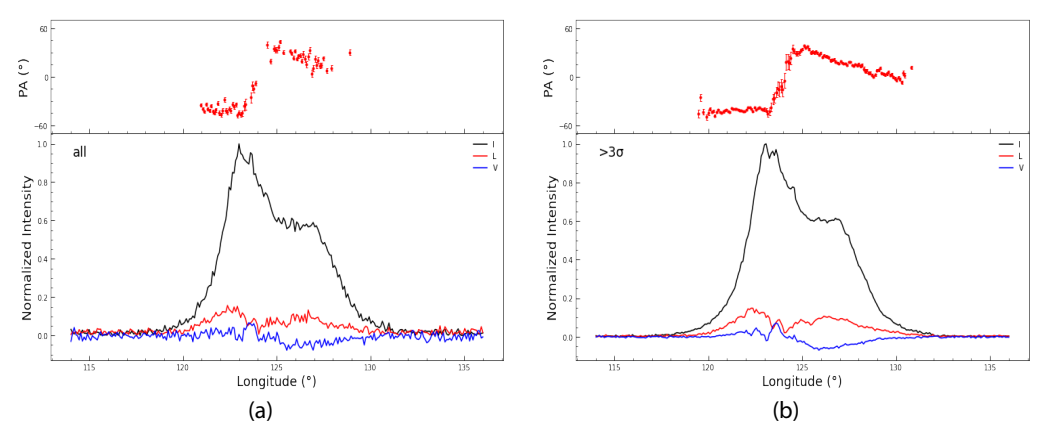


Figure 6. Two types of integrated pulse profiles are shown. Panel (a) displays the average profile from all pulses, while panel (b) presents the profile averaged from pulses exceeding $3\sigma_{\rm off}$ (three times the off-pulse region's rms value).

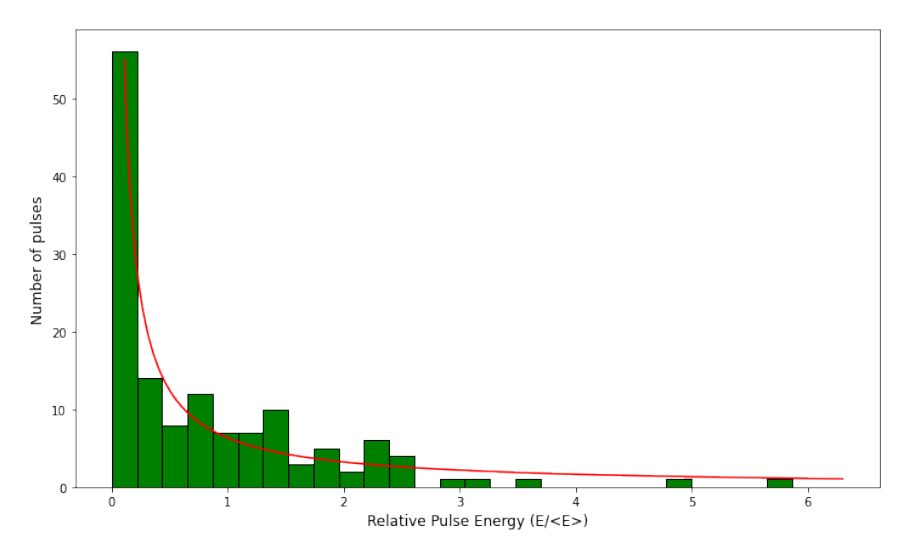


Figure 7. Relative energy distribution during the burst state of 146 single pulses. The vertical axis represents pulse counts and the horizontal axis shows relative energy. The data were fitted with a power-law model, yielding a chi-square test statistic of $\chi^2 = 18.61$ with 15 degrees of freedom, indicating a statistically acceptable fit.

3.7. The Profile Morphology of Single Pulses

Current theories of pulsar radio emission suggest coherent radiation originates from secondary electron-positron pair plasma near the polar cap, where electrostatic-current instabilities produce resonant plasma waves (Gangadhara et al. 2021). Analysis of single-pulse profiles provides crucial insights into the instantaneous state of relativistic particles through four key parameters: (1) peak longitude (phase of maximum intensity), (2) pulse width (determined using $3\sigma_{\rm off}$ threshold filtering of off-pulse noise), (3) relative energy intensity (following Ritchings 1976), and (4) The number of peaks in each pulse profile is determined using the method proposed by Guo et al. (2024). In this approach, one or more Gaussian functions are first applied to smooth the pulse profile, effectively suppressing noise and enhancing real structural features. Then, the rms value

of the off-pulse region is calculated, and a detection threshold is set at three times the rms value. Peaks that exceed this threshold are identified as significant. The number of such significant peaks is used to classify the pulse profile as single-peaked, double-peaked, or multi-peaked. The classification results are illustrated in Figure 10, where the red dashed lines represent the fitted curve composed of multiple Gaussian components.

The statistical distributions of these parameters (Table 2) reveal systematic differences among pulse types. While all categories exhibit comparable peak longitude ranges, the tabulated data indicates that both double-peaked and multipeaked pulses tend to have broader profiles and higher relative energies compared to single-peaked pulses. The consistent peak longitudes across different profile morphologies suggest the emission geometry remains stable, with profile variations

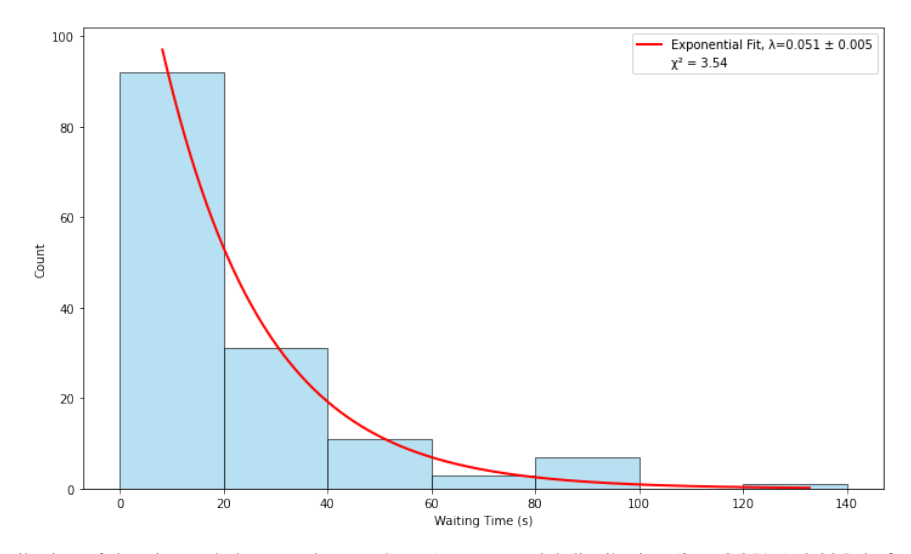


Figure 8. Distribution of time intervals between burst pulses. An exponential distribution ($\lambda = 0.051 \pm 0.005$) is fitted to the data.

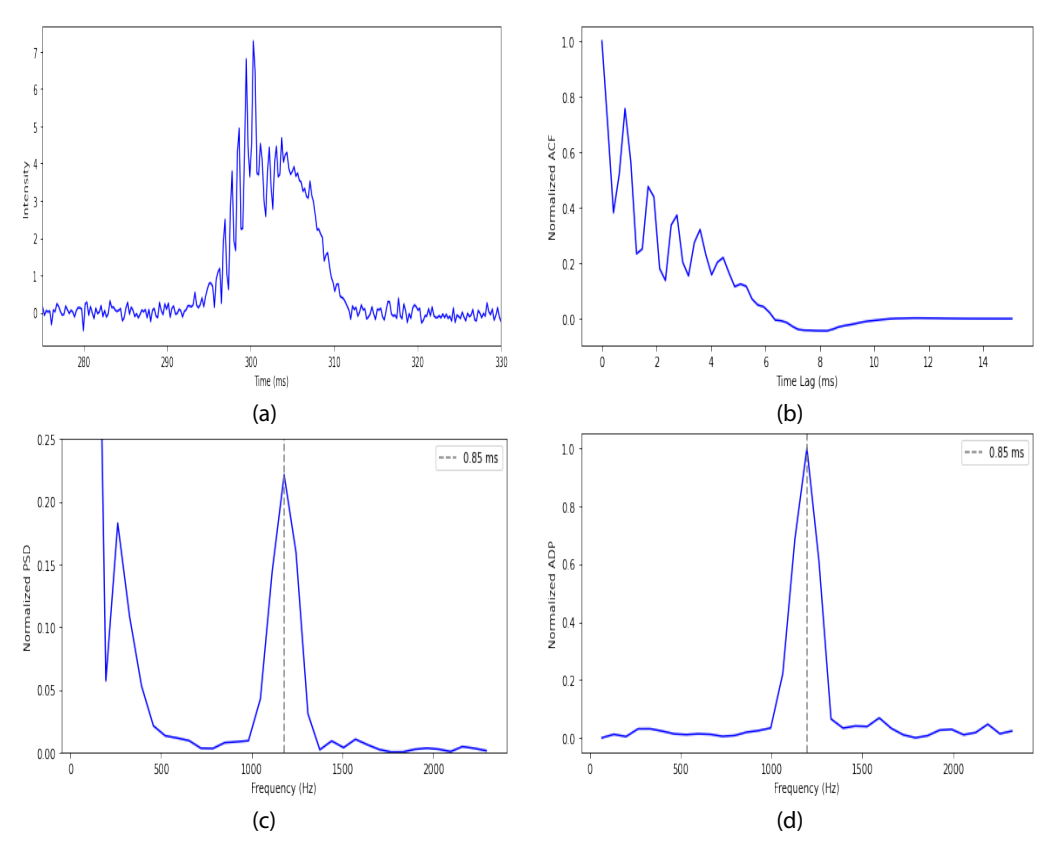
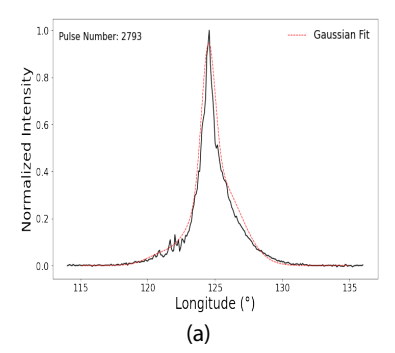


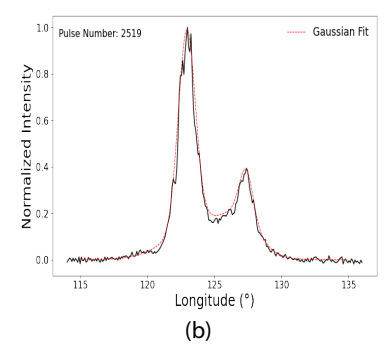
Figure 9. The microstructure, autocorrelation function (ACF), Fourier power spectral density (PSD) of the pulse, and power spectral density (ADP) of the ACF for pulse 950 are presented. Vertical dashed lines mark the frequency peaks in both the PSD and ADP panels.

likely arising from plasma turbulence or beam pattern effects (Gangadhara et al. 2021). This interpretation aligns with the phased-array radiation model, where local plasma density fluctuations can modify profile shapes without altering the global magnetospheric configuration.

3.7.1. Single-peaked Profile

During the observation period, 75 out of the 146 detected single pulses exhibited a single-peaked profile, as shown in Figure 10(a). The 75 single-peaked pulses had an average peak longitude of 124.95, an average relative energy of 0.89, and an





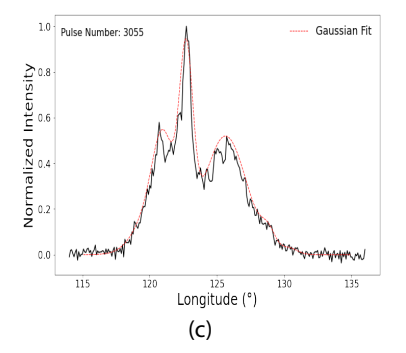


Figure 10. Schematic diagrams of three types of single pulse profiles: (a) single-peaked profile, (b) double-peaked profile, and (c) multi-peaked profile.

 Table 2

 Statistical Data of Three Types of Single Pulses

Parameter	Value
One-peak pulses $(N = 75)$	
Peak longitude	124°95 [121.03, 129.55]
Relative pulse energy $(E_i/\langle E \rangle)$	0.89[-0.07, 7.60]
Pulse width (W)	2.88 [0.09, 11.16]
Two-peak pulses $(N = 59)$	
Peak longitude	124°.12 [121.46, 130.96]
Relative pulse energy $(E_i/\langle E \rangle)$	1.26 [0.06, 3.87]
Pulse width (W)	6.40 [0.44, 11.34]
Multiple-peak pulses ($N = 12$)	
Peak longitude	123°74 [121.99, 126.65]
Relative pulse energy $(E_i/\langle E \rangle)$	1.14 [0.26, 2.38]
Pulse width (W)	7.50 [2.20, 10.81]

Note. Values represent median [minimum, maximum] ranges. Pulse width (W) indicates the effective pulse region width determined through threshold filtering. N indicates the number of pulses in each category.

average pulse width of 2.88. The statistical results are presented in Table 2.

Our analysis shows that most single-peaked pulses are characterized by narrow profiles and relatively low intensities, while a minority exhibit strong and broad features. The degree of linear polarization among these pulses ranges from 0% to 100%, with an average of approximately $28.2\% \pm 0.4\%$. Some single-peaked pulses display either left- or right-handed circular polarization. Notably, the single-peaked pulse numbered 2793 in Figure 4 predominantly exhibits left-handed circular polarization, accompanied by slight polarization reversal.

3.7.2. Double-peaked Profile

As shown in Figure 10(b), we detected 59 single pulses with double-peaked profiles during the observation period. These pulses consist of two components, with an average peak longitude of 124.12, an average relative energy of 1.26, and an

average pulse width of 6.40. Detailed statistical results are presented in Table 2.

Compared to their single-peaked counterparts, double-peaked pulses predominantly exhibit strong and broad emission features, although some also show narrow and weak radiation. The linear polarization degrees of these pulses range from 0% to 100%, with an average of approximately $28.5\% \pm 0.3\%$. Notably, the double-peaked pulse numbered 2519 exhibits repeated reversals in circular polarization direction, accompanied by an orthogonal mode jump at a phase of 122.5.

The circular polarization reversals observed in single pulse 2519 likely reflect complex conditions within the pulsar's magnetosphere, such as a non-uniform magnetic field or multipath propagation effects. According to Wang et al. (2012), the sign of circular polarization can reverse depending on the gradient of particle density along the rotational phase. This suggests that variations in plasma density and distribution within the magnetosphere may lead to changes in circular polarization characteristics. In addition, Petrova (2006) proposed that pulsar radio emission can be modeled as a superposition of two non-orthogonal polarization modes. These modes evolve due to propagation effects within the magnetosphere, such as wave mode coupling and cyclotron absorption. As waves pass through cyclotron resonance, they may become non-orthogonal. Pulse-to-pulse variations in polarization and intensity ratio are generally associated with temporal fluctuations in plasma flow. Therefore, the observed reversals in subpulse 2519 are consistent with plasma fluctuations and associated mode coupling processes.

3.7.3. Multi-peaked Profile

During the observation period, we detected 12 single pulses exhibiting multi-peaked profiles, each comprising three or more peaks (see Figure 10(c)). Our analysis reveals an average peak longitude of 123.74, an average relative energy of 1.14, and an average pulse width of 7.50 for these pulses. Detailed statistical results are presented in Table 2.

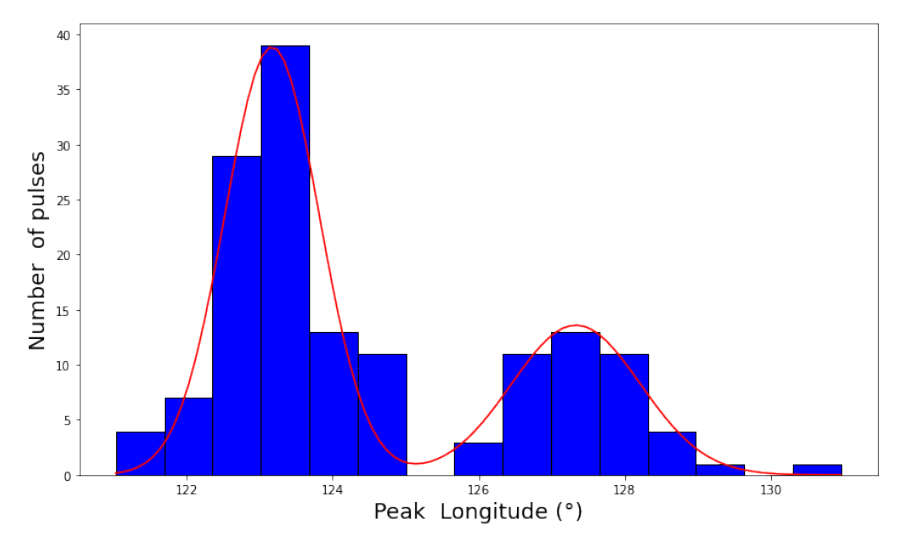


Figure 11. Histogram of peak longitudes fitted with a double Gaussian model.

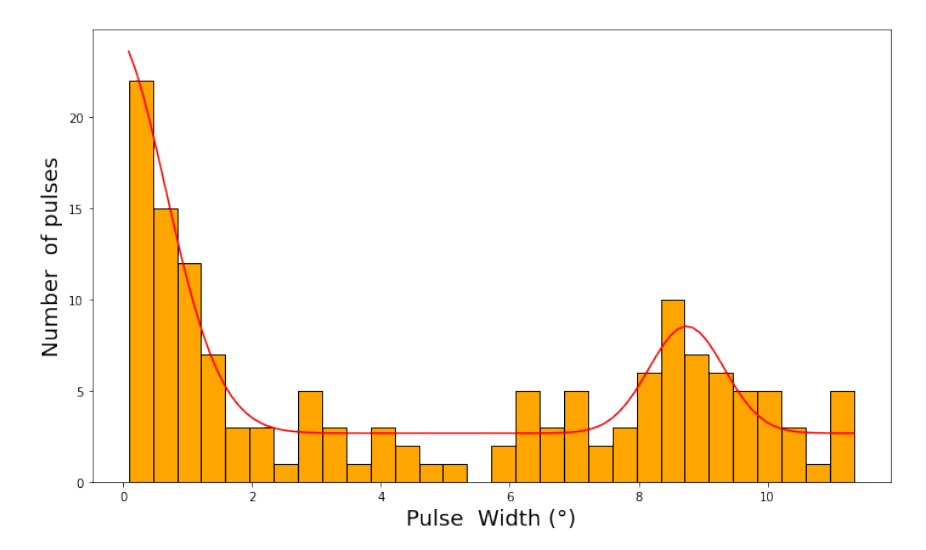


Figure 12. Histogram of pulse widths fitted with a mixed exponential-Gaussian model.

The number of multi-peaked pulses is significantly smaller than that of single- and double-peaked pulses. Overall, they exhibit features similar to those of double-peaked pulses, being predominantly broad and strong, with a small fraction showing weak and narrow characteristics. The degree of linear polarization of multi-peaked pulses ranges from 0% to 100%, with an average value of approximately $26.5\% \pm 0.6\%$. Notably, distinct orthogonal mode jumps have been observed in most strong multi-peaked pulses, mainly occurring between phases 122° and 127° , accompanied by transitions between left-handed and right-handed circular polarization. For example, the multipeaked pulse numbered 3055 exhibits multiple reversals in circular polarization direction.

To explore the relationships between pulse energy, pulse width, and peak longitude, we generated Figures 11, 12, and

13. Figure 11 shows the distribution of peak longitudes, which is well described by a double Gaussian function. The K-S test yields D=0.09 and P=0.18, indicating that peak longitudes are primarily concentrated in two regions: $122^{\circ}-124^{\circ}$ and 127° . This suggests that the single pulses of RRAT J2325 -0530 are mainly composed of single-peaked and double-peaked profiles, which is consistent with our statistical classification. In addition, the boundary between the two Gaussian components lies near 125° , closely matching the typical phase boundary identified in our component-based separation of double- and multi-peaked pulses.

Figure 12 presents the distribution of pulse widths, where narrower pulses are better fitted by an exponential decay model, while broader pulses are better described by a Gaussian model. The K-S test results (D = 0.08 and P = 0.41) validate

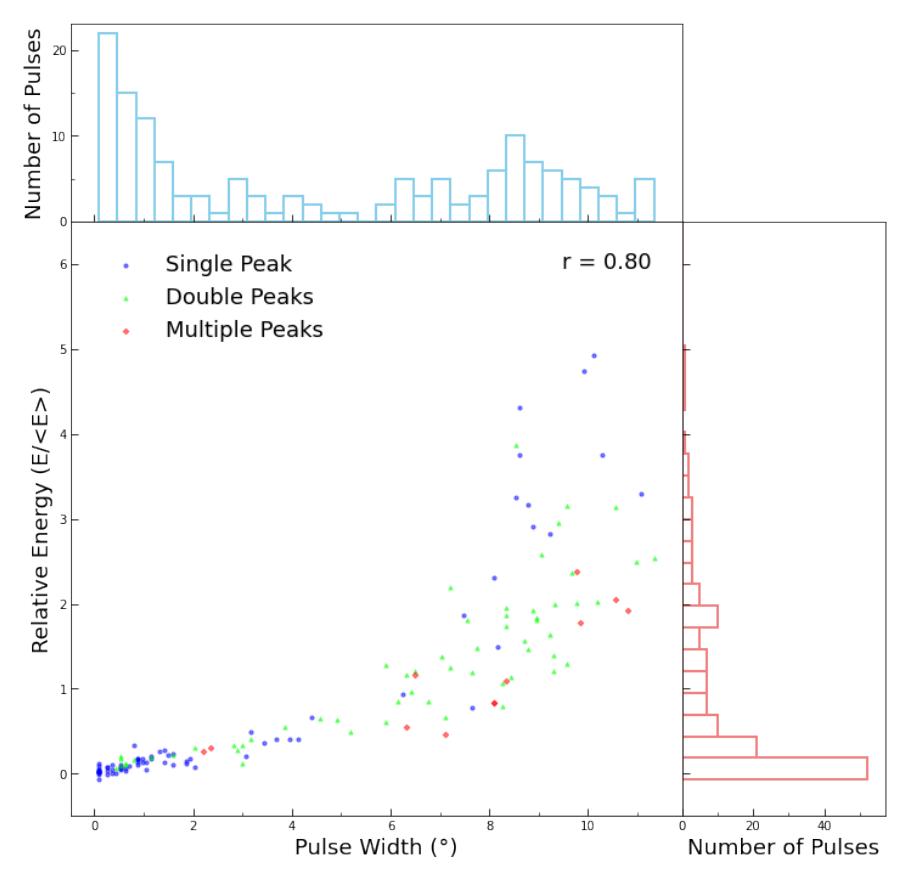


Figure 13. Correlation between relative energy and pulse width, showing a significant positive correlation (r = 0.80).

the suitability of this fitting approach. The data indicate that narrower pulses are mostly single-peaked, but also include some double-peaked and a few multi-peaked pulses, exhibiting exponential decay characteristics. In contrast, broader pulses are predominantly double-peaked, with some multi-peaked and very few single-peaked pulses, following a Gaussian distribution. This distribution implicitly reflects a positive correlation between the number of pulse components and pulse width.

Figure 13 shows a significant positive correlation between relative energy and pulse width, with a correlation coefficient of r=0.80. This suggests that multi-peaked and double-peaked pulses generally have larger widths and higher energies. Notably, all pulse types can be categorized into two groups: narrow and weak pulses, and broad and strong pulses, implying potential differences in their radiation mechanisms. Additionally, no significant correlations were found between peak longitude and relative energy, or between pulse width and peak longitude.

The characteristics of multi-peaked pulses can be explained by several mechanisms within the pulsar magnetosphere:

1. Structured Emission Mechanism in the Polar Cap Region. According to Spitkovsky (2006), pulsar radio emission might result from two different emission mechanisms within the magnetosphere. One operates in the inner magnetosphere and is related to the pair-production process near the polar caps. The other operates near the light cylinder and is specific to pulsars with high magnetic field strength in that region. Multipeaked single pulses are more likely generated by structured radiation patterns in the polar cap region (such as multiple emission beams or plasma oscillations), while the light cylinder region may contribute to both radio-wave and high-energy radiation (e.g., X-rays).

- 2. Magnetospheric Current Sheet Emission. The research by Philippov & Kramer (2022) suggests that high-energy radiation in pulsars is likely produced in the magnetospheric current sheet beyond the light cylinder. The complex structure and dynamic evolution of the current sheet might lead to multi-peaked pulse profiles. The interaction between the current sheet and the surrounding plasma could cause variations in the emission characteristics, resulting in multiple peaks in the pulse profile.
- 3. Particle Acceleration and Synchrotron Radiation. In the model proposed by Giraud and Giraud & Pétri (2021), both curvature and synchrotron radiation are considered

to operate within the magnetosphere. Radio emission arises from dipolar regions above the polar caps, while gamma-ray energy emanates from the slot gaps near the separatrix between closed and open field lines. The multi-peaked pulses might be associated with the acceleration of particles in different regions of the magnetosphere and their subsequent synchrotron radiation. The specific distribution of particle energies and magnetic field configurations could lead to the formation of multiple peaks in the pulse profile.

4. Comparison and Discussion

4.1. Comparison

This section is divided into two parts: (1) A detailed comparison between the traditional polar cap model (Ruderman & Sutherland 1975) and the partially coherent emission model (Oswald et al. 2023) in the context of the radiation properties of RRAT J2325-0530; (2) A comprehensive comparison between the results of this study and observations from other RRAT sources.

4.1.1. Comparison of Radiation Models

The traditional polar cap model (Ruderman & Sutherland 1975) posits that pulsar emissions originate from the polar cap region, where high-energy particles are accelerated along open magnetic field lines. While this model offers a foundational framework for understanding periodic pulsar emissions and single-peaked pulse profiles, it has limitations when explaining the complex radiation characteristics observed in RRAT J2325–0530. Notably, it struggles to account for the multi-peaked pulse profiles, significant polarization reversals, and the extremely high nulling fraction coupled with sporadic strong pulses.

In contrast, the partially coherent emission model (Oswald et al. 2023) provides a more nuanced explanation. This model suggests that pulsar radio emissions arise from localized regions within the magnetosphere, formed by particle beams excited through intermittent discharges in magnetic gaps. These regions can produce coherent radiation through partial coherence mechanisms. The model's flexibility allows it to better accommodate the multi-peaked pulses and polarization reversals observed in RRAT J2325–0530. However, the model's predictions can vary depending on the assumed parameters for the emission regions and particle beams, indicating a need for further refinement.

4.1.2. Comparison with Other RRATs

We conducted a systematic comparison of RRAT J2325 -0530 with other well-studied RRATs in the literature. Guo et al. (2024) found that the burst-state energy distribution of

J1856–0306 follows an exponential decay, which is inconsistent with the power-law behavior observed in J2325–0530. However, both sources exhibit a strong positive correlation between pulse energy and width, and their single-pulse PA distributions are highly scattered and complex, consistent with the polarization characteristics of J2325–0530. Notably, the average PA curve of J1856+0306 shows a classical "S"-shaped variation in agreement with the RVM, in stark contrast to the chaotic average PA curve of J2325–0530. This discrepancy suggests that the RVM does not universally describe RRAT polarization behavior and that the radiation of J2325–0530 may arise from more complex, multi-scale magnetospheric processes near the polar cap.

In terms of radiation intermittency, the pulse window occupancy of J2325–0530 is only 4.23%, which is comparable to 3.12% reported for RRAT J1918–0449 (Chen et al. 2022), reinforcing the highly sporadic and random emission nature of many RRATs. In contrast, Zhang et al. (2024) and Zhong et al. (2024) reported long sequences of continuous bursts in J1913 +1330, which are rarely seen in J2325–0530. The emission of J2325–0530 is instead dominated by isolated or paired bursts over one or two rotations. This contrast hints at intrinsic differences in magnetospheric stability and emission triggering mechanisms across RRATs. The presence of long burst trains in J1913+1330 may indicate a quasi-stable particle acceleration process, while the sporadic activity of J2325–0530 suggests a more stochastic or threshold-driven emission regime.

Regarding microstructure, the quasi-periodicity P_{μ} of J2325 -0530 agrees well with the relation $P_{\mu}\approx 10^{-3}P$, consistent with results from J1918-0449 (Chen et al. 2022) and J1913 +1330 (Tang et al. 2025). Interestingly, the empirical relation $\tau_{\mu}\approx 0.5P_{\mu}$ between micropulse width τ_{μ} and P_{μ} is only confirmed in J2325-0530 and J1918-0449. The absence of this relationship in J1913+1330 may suggest different underlying emission coherence scales, or observational limitations such as burst duration, signal-to-noise ratio, or selection effects that hinder microstructure detection. Alternatively, this may point to different physical regimes governing microstructure generation in RRATs with extended burst trains.

In terms of polarization, the degrees of linear and circular polarization in J1913+1330 are 28% and -0.6%, respectively, consistent with our measurements for J2325-0530. Both sources show highly scattered PA distributions that deviate from classical RVM fits, reinforcing the complexity of their single-pulse polarization signatures. In J1913+1330, the linear polarization fraction (L/I) of some single pulses can approach 100%, and multiple reversals of circular polarization have been observed, highlighting the diversity and complexity of emission mechanisms in RRATs at the single-pulse level (Zhang et al. 2024; Zhong et al. 2024).

4.2. Discussion

4.2.1. Emission Geometry and Radiation Mechanisms

Our observational data offer crucial insights that help distinguish between these two models.

- 1. Multi-peaked Pulses. The traditional polar cap model assumes an axisymmetric structure, with discharge sparks uniformly distributed along the polar cap boundary and an ideal dipolar magnetic field configuration. Within this idealized framework, pulsar emission typically manifests as single-peaked or double-peaked profiles. However, RRAT J2325—0530 exhibits partially multi-peaked pulses, which align better with the predictions of the partially coherent emission model (Oswald et al. 2023). The multiple peaks in the pulse profile can be interpreted as emissions from distinct localized regions within the magnetosphere, which may be intermittently activated due to plasma instabilitiesphenomena that are difficult to reconcile within the traditional polar cap model.
- 2. Polarization Reversals. The significant polarization reversals observed in multi-peaked pulses align more closely with the collective plasma radiation model proposed by Gangadhara et al. (2021). This model demonstrates that when secondary electron-positron pairs form phased arrays under the influence of plasma waves, the resulting coherent curvature radiation naturally produces polarization sign reversals correlated with polarization angle swings. As the line of sight traverses through emission regions with varying polarization characteristics, the observed polarization properties exhibit corresponding changes. Such dynamic polarization behavior is not readily explainable by the traditional polar cap model.
- 3. Energy Distribution. The energy distribution of individual pulses from RRAT J2325-0530 appears to follow a power-law trend and demonstrates a statistically significant correlation with pulse width. This characteristic shows marked differences from the log-normal distributions observed in canonical pulsars like Vela (Cairns et al. 2001). These discrepancies may suggest distinct emission mechanisms: while the log-normal distribution of Vela is broadly consistent with predictions from Stochastic Growth Theory, where the emission likely originates from stochastic wave-particle interactions in marginally stable plasma (Cairns et al. 2001), the powerlaw distribution of RRAT J2325-0530 could indicate a non-thermal particle acceleration process exhibiting scale-free properties. The partially coherent radiation model offers one plausible interpretive framework, suggesting that the observed energy distribution might reflect turbulence- or reconnection-driven acceleration

- processes in the magnetosphere, with the pulse-width correlation potentially relating to spatial or temporal scales of the emission regions. In contrast, conventional polar cap gap models based on steady-state acceleration assumptions face considerable challenges in accounting for such variability. These characteristics imply that RRATs may involve a particular type of magnetospheric activity, potentially incorporating bursty or intermittent energy release mechanisms.
- 4. Distribution of Peak Longitude and Component Boundary. The observed peak longitude exhibits a bimodal distribution, mainly concentrated in the regions of 122°-124° and 127°, with a noticeable drop in energy around 125°. This is difficult to explain using the traditional polar cap model, which typically assumes an axisymmetric distribution of discharge sparks in the polar cap region, expecting more uniform radiation. In contrast, certain coherent radiation models that consider multiple finite-coherence sub-emission regions within the magnetosphere can naturally explain this structure. Variations in coherence among these sub-sources at different rotational phases lead to constructive interference enhancing the radiation in the two main peak regions, while reduced coherence or destructive interference near 125° causes a decrease in radiation energy, forming a clear component boundary. This explanation is highly consistent with our statistical classification results and provides a reasonable physical mechanism for the nonuniform distribution of peak longitude.

In conclusion, while the traditional polar cap model provides a basic framework for understanding pulsar emissions, it is limited in explaining the complex radiation properties observed in RRAT J2325-0530. The partially coherent emission model offers a more comprehensive explanation for the observed multi-peaked pulses, polarization reversals, and energy distribution characteristics. However, further refinements and detailed comparisons with observational data are necessary to better constrain the parameters and predictions of the partially coherent emission model. Future research should focus on enhancing the theoretical framework of the partially coherent emission model and exploring its implications for pulsar magnetosphere physics. This will involve continued multi-wavelength observations and advanced simulations to deepen our understanding of the physical processes underlying RRAT J2325-0530's radiation properties.

4.2.2. Burst Trigger Mechanism and Nulling Behavior

The absence of correlation between burst energy and null duration in RRAT J2325-0530 challenges conventional pulsar emission models where energy is expected to accumulate during quiescent periods. This behavior suggests a threshold-

dependent activation process, where bursts are triggered only when local magnetospheric conditions (such as plasma density or magnetic field geometry) reach critical thresholds, independent of preceding inactivity duration. The extreme nulling fraction implies that the source operates near physical limits of radio emission viability, where stochastic magnetospheric disturbances—rather than deterministic energy storage—dominate the bursting behavior. These characteristics align with the sporadic emission patterns first identified in RRATs by McLaughlin et al. (2006), while contrasting with the more predictable nulling pulsars studied by Burke-Spolaor & Bailes (2009).

The observed behavior may reflect either localized plasma injections in a magnetosphere nearing the death line (Beskin & Istomin 2022), or unusual pair-production processes in underluminous pulsars. In such scenarios, small-scale magnetic reconnections or starquake-induced plasma injections could generate bursts without requiring prolonged energy accumulation. This would explain the random energy distribution, while maintaining compatibility with the rotating vector model's polarization signatures. Similar sporadic emission has been observed in other extreme pulsar populations (Lynch et al. 2013), suggesting RRAT J2325–0530 represents an important transitional case between active pulsars and radio-quiet neutron stars.

5. Summary and Prospect

This study utilizes the high-sensitivity polarization observation data from the FAST to conduct a comprehensive analysis of the radiation characteristics of RRAT J2325-0530. The main findings include:

- 1. Three distinct pulse profile morphologies (single-peaked, double-peaked, and multi-peaked) were observed, with the multi-peaked pulses exhibiting significant polarization reversal features (average linear polarization degree of $27.5\% \pm 0.3\%$) and relatively broad pulse widths (7.50 ± 0.82) . The relative energy distribution follows a power-law trend and shows a strong correlation with pulse width (r = 0.80).
- 2. The waiting time distribution follows a Poisson process with a time constant $\lambda=0.051\pm0.005$, corresponding to a burst rate of $184\pm18\,\mathrm{hr}^{-1}$. Microstructure analysis reveals that the quasi-periodicity P_μ and microstructure width τ_μ follow the relations $\tau_\mu\approx0.5P_\mu$ and $P_\mu\approx10^{-3}P$.
- 3. The diverse pulse profile characteristics and their polarization properties challenge existing radiation models, providing new insights for pulsar magnetospheric physics research. The results particularly support the plasma beam instability model proposed by Gangadhara et al. (2021), while the randomly occurring pulse

intervals suggest that its magnetospheric dynamical processes are more complex than current theoretical predictions.

Future research should focus on the following aspects:

- 1. According to the dual-component emission model proposed by Spitkovsky (2006), the light cylinder region in a pulsar's magnetosphere generates high-energy radiation such as X-rays, providing the theoretical foundation for multi-wavelength observations. By combining FAST's radio observations with the detection capabilities of X-ray telescopes like NICER, we can simultaneously capture both the radio emissions from the polar cap region and the high-energy radiation from the light cylinder region. This approach enables a comprehensive understanding of the radiation characteristics and their correlations across different magnetospheric regions.
- 2. Another crucial direction for future research is extending the monitoring time. This will increase the chances of capturing rare radiation events, which are vital for establishing statistical significance. By collecting more data on these infrequent but informative occurrences, we can enhance our understanding of the physical mechanisms that underpin RRATs' radiation properties.
- 3. Incorporating the precise parameters obtained from this study into advanced particle simulations, such as Particle-in-Cell (PIC) methods (Cruz et al. 2024; Song & Tamburini 2024; Soudais et al. 2024), offers a promising path for future research. This approach can significantly improve our comprehension of the generation mechanisms behind multi-peaked pulses. Furthermore, it may reveal universal patterns among RRATs with similar features, ultimately advancing our knowledge of pulsar radiation physics under extreme conditions.

Acknowledgments

This study was conducted using observational data from the Five-hundred-meter Aperture Spherical radio Telescope (FAST), a major national scientific and technological infrastructure facility in China operated and maintained by the National Astronomical Observatories of the Chinese Academy of Sciences (CAS). The data used in this work were obtained through the FAST project PT2021_0117, led by Professor Xiangdong Li.

This research was supported by the National Key Research and Development Program of China (No. 2022YFC2205202); the National Natural Science Foundation of China (NSFC, Basic Science Center Program, grant No. 12288102); the NSFC (FAST Special Project, grant No. 12041304); the

"Tianshan Talent Program" Team Project of the Xinjiang Uygur Autonomous Region (Project No. 2023TSYCTD0013); the Guizhou Provincial Science and Technology Projects (No. QKHFQ[2023]003 and No. QKHPTRC-ZDSYS[2023]003); and the NSFC (grant No. 12373114).

The authors would like to thank Professor Jinlin Han from the National Astronomical Observatories of CAS for his helpful discussions and valuable suggestions.

References

Abhishek, N., Tanushree, N., Hegde, G., & Konar, S. 2022, JApA, 43, 75

```
Barnard, J. J., & Arons, J. 1986, ApJ, 302, 138
Beskin, V. S., & Istomin, A. Y. 2022, MNRAS, 516, 5084
Beskin, V. S., & Philippov, A. A. 2012, MNRAS, 425, 814
Bezuidenhout, M. C., Barr, E., Caleb, M., et al. 2022, MNRAS, 512, 1483
Blaskiewicz, M., Cordes, J. M., & Wasserman, I. 1991, ApJ, 370, 643
Burke-Spolaor, S., & Bailes, M. 2009, MNRAS, 395, 410
Burke-Spolaor, S., & Bailes, M. 2010, MNRAS, 402, 855
Cairns, I. H., Johnston, S., & Das, P. 2001, ApJL, 563, L65
Chen, J. L., Wen, Z. G., Yuan, J. P., et al. 2022, ApJ, 934, 24
Cordes, J. M. 2013, ApJ, 775, 47
Cruz, F., Grismayer, T., Torres, R., et al. 2024, A&A, 690, A229
Cui, B. Y., Boyles, J., McLaughlin, M. A., & Palliyaguru, N. 2017, ApJ,
Dong, F. A., Crowter, K., Meyers, B. W., et al. 2023, MNRAS, 524, 5132
Gangadhara, R. T. 2005, ApJ, 628, 923
Gangadhara, R. T., Han, J. L., & Wang, P. F. 2021, ApJ, 911, 152
Giraud, Q., & Pétri, J. 2021, A&A, 654, A86
Good, D. C., Andersen, B. C., Chawla, P., et al. 2021, ApJ, 922, 43
Guo, Q., Kong, M., Wang, P. F., Yan, Y., & Zhou, D. J. 2024, MNRAS,
   530, 2433
Han, J. L., Wang, C., Wang, P. F., et al. 2021, RAA, 21, 107
Hotan, A. W., van Straten, W., & Manchester, R. N. 2004, PASA, 21, 302
Hsu, J. A., Jiang, J. C., Xu, H., Lee, K. J., & Xu, R. X. 2023, MNRAS, 518, 1418
Karako-Argaman, C., Kaspi, V. M., Lynch, R. S., et al. 2015, ApJ, 809, 67
Karastergiou, A., Hotan, A. W., van Straten, W., McLaughlin, M. A., &
   Ord, S. M. 2009, MNRAS, 396, L95
Keane, E. F., Kramer, M., Lyne, A. G., Stappers, B. W., & McLaughlin, M. A.
   2011, MNRAS, 415, 3065
```

```
2024, NatAs, 8, 230
Kravtsov, I. P., Zakharenko, V. V., Vasylieva, I. Y., et al. 2020, RPRA,
Lange, C., Kramer, M., Wielebinski, R., & Jessner, A. 1998, A&A, 332, 111
Lynch, R. S., Boyles, J., Ransom, S. M., et al. 2013, ApJ, 763, 81
McLaughlin, M. A., Lyne, A. G., Lorimer, D. R., et al. 2006, Natur, 439, 817
Meyers, B., Tremblay, S. E., Bhat, N. D. R., & Shannon, R. M. 2016, A Low
   Frequency Study of Rotating Radio Transients, MWA Proposal
  id.2016B-02,
Meyers, B. W., Tremblay, S. E., Bhat, N. D. R., et al. 2019, PASA, 36, e034
Oswald, L. S., Karastergiou, A., & Johnston, S. 2023, MNRAS, 525, 840
Patel, C., Agarwal, D., Bhardwaj, M., et al. 2018, ApJ, 869, 181
Petrova, S. A. 2006, MNRAS, 368, 1764
Philippov, A., & Kramer, M. 2022, ARA&A, 60, 495
Philippov, A., Timokhin, A., & Spitkovsky, A. 2020, PhRvL, 124, 245101
Radhakrishnan, V., & Cooke, D. J. 1969, ApJL, 3, 225
Ritchings, R. T. 1976, MNRAS, 176, 249
Ruderman, M. A., & Sutherland, P. G. 1975, ApJ, 196, 51
Samodurov, V. A., Tyul'bashev, S. A., Toropov, M. O., & Logvinenko, S. V.
  2022, ARep, 66, 341
Samodurov, V. A., Tyul'bashev, S. A., Toropov, M. O., et al. 2023, ARep,
Song, H.-H., & Tamburini, M. 2024, MNRAS, 530, 2087
Soudais, A., Cerutti, B., & Contopoulos, I. 2024, A&A, 690, A170
Spitkovsky, A. 2006, ApJL, 648, L51
Tang, Z., Zhang, S., Wang, J., Yang, X., & Wu, X. 2025, MNRAS, 539, 1352
Tyul'bashev, S. A., Pervukhin, D. V., Kitaeva, M. A., et al. 2022, A&A,
Tyul'bashev, S. A., Tyul'bashev, V. S., & Malofeev, V. M. 2018a, A&A,
  618, A70
Tyul'bashev, S. A., Tyul'bashev, V. S., Malofeev, V. M., et al. 2018b, ARep,
  62. 63
van Straten, W., & Bailes, M. 2011, PASA, 28, 1
Wang, P. F., Wang, C., & Han, J. L. 2012, MNRAS, 423, 2464
Wang, P. F., Wang, C., & Han, J. L. 2014, MNRAS, 441, 1943
Weltevrede, P., Stappers, B. W., Rankin, J. M., & Wright, G. A. E. 2006,
   ApJL, 645, L149
Yuen, R. 2024, A&A, 683, A108
Zhang, B., Gil, J., & Dyks, J. 2007, MNRAS, 374, 1103
Zhang, S. B., Geng, J. J., Wang, J. S., et al. 2024, ApJ, 972, 59
Zhong, W., Zhi, Q., Lu, J., et al. 2024, MNRAS, 527, 4129
Zhou, D. J., Han, J. L., Xu, J., et al. 2023, RAA, 23, 104001
```

Kramer, M., Liu, K., Desvignes, G., Karuppusamy, R., & Stappers, B. W.